



## **Towards autonomous inland shipping: a manoeuvring model in confined waterways**

Downloaded from: <https://research.chalmers.se>, 2024-07-17 18:48 UTC

Citation for the original published paper (version of record):

Zhang, C., Ma, Y., Thies, F. et al (2024). Towards autonomous inland shipping: a manoeuvring model in confined waterways. Ships and Offshore Structures, In Press.  
<http://dx.doi.org/10.1080/17445302.2024.2358284>

N.B. When citing this work, cite the original published paper.



## Towards autonomous inland shipping: a manoeuvring model in confined waterways

Chengqian Zhang, Yucong Ma, Fabian Thies, Jonas W. Ringsberg & Yihan Xing

**To cite this article:** Chengqian Zhang, Yucong Ma, Fabian Thies, Jonas W. Ringsberg & Yihan Xing (27 May 2024): Towards autonomous inland shipping: a manoeuvring model in confined waterways, Ships and Offshore Structures, DOI: [10.1080/17445302.2024.2358284](https://doi.org/10.1080/17445302.2024.2358284)

**To link to this article:** <https://doi.org/10.1080/17445302.2024.2358284>



© 2024 The Author(s). Published by Informa UK Limited, trading as Taylor & Francis Group



Published online: 27 May 2024.



Submit your article to this journal [↗](#)



Article views: 182



View related articles [↗](#)



View Crossmark data [↗](#)

# Towards autonomous inland shipping: a manoeuvring model in confined waterways

Chengqian Zhang<sup>a</sup>, Yucong Ma<sup>b</sup>, Fabian Thies<sup>a</sup>, Jonas W. Ringsberg<sup>a</sup> and Yihan Xing<sup>b</sup>

<sup>a</sup>Division of Marine Technology, Department of Mechanics and Maritime Sciences, Chalmers University of Technology, Gothenburg, Sweden;

<sup>b</sup>Department of Mechanical and Structural Engineering and Materials Science, University of Stavanger, Stavanger, Norway

## ABSTRACT

Autonomous inland water vessels are essential for promoting intelligent and sustainable waterborne transport. An accurate ship manoeuvring model ensures reliable control strategies and enhances navigation safety. Although ship manoeuvrability models have existed for decades, few studies address shallow and restricted waters. This study introduces a manoeuvring model for inland water vessels, accounting for confinement effects on ship motion. The Manoeuvring Modelling Group (MMG) model in open water serves as the baseline, incorporating empirical methods for shallow water and bank effects. This approach aims to provide a fast and accurate prediction of vessel motion response. The model was validated with free-running experimental data of a pusher-barge model from turning tests at three water depths. Additional case studies highlight shallow water impact compared to infinite water performance under bank effects. Finally, course-keeping case studies are presented, integrating a Proportional-Derivative controller with combined river current and bank-induced forces..

## ARTICLE HISTORY

Received 15 December 2023  
Accepted 12 April 2024

## KEYWORDS

Confinement effect; inland waterways; manoeuvring prediction; autonomous vessel; motion control

## Nomenclature


$A_R$	Rudder area [m <sup>2</sup> ]
$B$	Ship beam [m]
$C_B$	Ship block coefficient [-]
$C_F$	Frictional resistance coefficient [-]
$C_W$	Wave resistance coefficient [-]
$D_p$	Propeller diameter [m]
$Fr$	Froude number [-]
$Fr_h$	Depth Froude number [-]
$H$	Water depth [m]
$J$	Propeller advance ratio [-]
$L$	Ship length [m]
$N_B, N_H, N_R$	Yaw moment components from bank effect, ship hull, and rudders [kNm]
$n_p$	Propeller revolution speed [rpm]
$K_T$	Propeller thrust coefficient [-]
$k$	Form factor [-]
$k_0, k_1, k_2$	Fitting coefficient for $K_T$ [-]
$Re$	Reynolds Number [-]
$r$	Yaw rate [rad/s]
$S_w$	Ship wetted surface area [m <sup>2</sup> ]
$s$	Propeller slip ratio [-]
$T$	Ship draught [m]
$t$	Thrust deduction factor [-]
$U$	Ship speed [m/s]
$U_C$	River current speed [m/s]
$U_R$	Total inflow speed at rudder [m/s]
$u$	Longitudinal ship speed [m/s]
$u_R$	Longitudinal rudder inflow speed [m/s]
$v$	Lateral ship speed at centre of gravity [m/s]
$v_R$	Lateral rudder inflow speed [m/s]
$W_C$	Channel width [m]
$w_{p0}$	Wake fraction at propeller during straight motion [-]
$w_p$	Wake fraction at propeller during manoeuvring [-]
$w_R$	Wake fraction at rudder [-]
$X_B, X_H, X_P, X_R$	Surge force components from bank effect, ship hull, propellers, and rudders [kN]
$Y_B, Y_H, Y_R$	Sway force components from bank effect, ship hull, and rudders [kN]
$y_B$	Non-dimensional quantity for ship-bank distance [-]

$y_s, y_p$	Distance from mid-ship to starboard bank and portside bank [m]
$\alpha_H$	Rudder force increase factor [-]
$\alpha_R$	Effective inflow angle at the rudder [rad]
$\beta$	Drift angle at midship [rad]
$\beta_p$	Inflow angle to rudder during manoeuvring [rad]
$\delta$	Rudder angle [rad]
$\varepsilon$	Ratio of wake fraction at rudder to propeller [-]
$\Lambda$	Rudder aspect ratio [-]
$\rho$	Water density [kg/m <sup>3</sup> ]
$\psi$	Ship heading angle [rad]

## 1. Introduction

Inland shipping is a transportation mode that utilises inland waterways, including canals, rivers, and lakes, for passengers and freight transportation (Wiegman et al. 2015). With a total length of over 40,000 kilometres, the European inland waterways connect hundreds of major European cities. Nevertheless, these waterways have been underutilised during the past decades, accounting for only 6% of the European inland freight transportation based on tonne-kilometres (Eurostat 2022) and market share (Sys et al. 2020). Given an increased utilisation, inland shipping has great potential to become an energy-efficient and sustainable alternative to road-based transportation, which has dominated the greenhouse gas emission in the freight transportation networks in Europe over the past few decades. The European Commission believes promoting inland waterways can reduce the number of tonne-kilometres by road transport (trucks) and reduce the burden of road congestion (European Commission 2023). Besides, inland shipping is also advantageous in energy consumption and noise compared to road and railway transportation (Perčić et al. 2021). It is considered one of the most cost-effective transportation methods in terms of infrastructural and external costs (United Nation 2015).

Shifting from road-based towards inland waterways transportation will result in a more climate-friendly transportation sector

**CONTACT** Chengqian Zhang  chengqian.zhang@chalmers.se Department of Mechanics and Maritime Sciences, Division of Marine Technology, Chalmers University of Technology, Hörsalsvägen 7A, 412 96 Gothenburg , Sweden

© 2024 The Author(s). Published by Informa UK Limited, trading as Taylor & Francis Group

This is an Open Access article distributed under the terms of the Creative Commons Attribution License (<http://creativecommons.org/licenses/by/4.0/>), which permits unrestricted use, distribution, and reproduction in any medium, provided the original work is properly cited. The terms on which this article has been published allow the posting of the Accepted Manuscript in a repository by the author(s) or with their consent.

and reduce overall costs. This can be further benefited by combining low-carbon (Hansson et al. 2019) or fossil-free fuels and a high level of autonomy as future solutions. In line with this initiative, the EU-funded project AUTOBarge (<https://etn-autobarge.eu>) aims to improve the competitiveness of inland waterways transport by building the next-generation waterborne network for cargo and passenger transportation, utilising autonomous inland waterway vessels (IWVs). An important part of this project is to provide a reliable and robust numerical simulation model to capture and analyse the characteristics and performance of various IWVs (Zhang et al. 2023). These models will further enable researchers and industry to study the unique challenges in confined waterways and support the development of autonomous control systems to tackle these challenges, which is critical in promoting waterborne transport in an intelligent and sustainable manner.

Inland waterway transportation is generally very safe as these vessels sail at a relatively low speed. However, the operation of IWVs in confined water is still limited by canal width, water level variations, and water current (Xing et al. 2013; Christodoulou et al. 2020). Their operation and navigation environments are distinguished from marine vessels sailing on unconstrained deep waters (Zou and Larsson 2013). Consequently, detailed assessments must be conducted when applying the seagoing-ship-based prediction methods on IWVs (Liu et al. 2015). New test manoeuvres and procedures are needed to improve the predictions of the IWVs' dynamics better (Landsburg et al. 2005; Liu et al. 2014).

The change of water depth affects the pressure distribution around the hull and significantly affects the motion and manoeuvrability of IWVs (Hofman and Kozarski 2000). This is specifically obvious in shallow water. The reduced water depth induced an increased draught on the vessel, i.e. squat, and further influenced the vessel's hydrodynamic forces and trajectory during manoeuvring. Pompée (2015) defines shallow water effects when the water depth ( $H$ ) is lower than four times the draught ( $T$ ), while Vantorre (2003) states that the shallow water effects become noticeable when the depth-to-draught ratio  $H/T < 3.0$ . A reduced water depth primarily affects the IWVs' resistance in the ship's forward direction due to the squat effect and increase in wave height (Jachowski 2008). It may either increase (Kim et al. 2022) or decrease (Yoshimura and Sakurai 1988) the tactical diameter in a ship's turning circle. However, the shallow water effect is mainly studied on large marine vessels (Liu et al. 2015), commonly wider in beam and less agile than inland vessels. Therefore, the shallow water effect on IWVs is yet to be clarified.

In addition, IWVs operate on narrow waterways. According to the Dutch Ministry of Infrastructure and Water Management, the lowest inland waterway's width is two times, three times, and four times the ship's beam for the single-lane, narrow double-lane, and double-lane channels, respectively (Rijkswaterstaat 2011). Therefore, a high level of manoeuvrability is necessary when the vessels pass through densely installed artificial structures such as locks, terminals, and bridge pillars along these narrow channels (Liu et al. 2015). Consequently, in contrast to marine vessels that commonly equip single-rudder single-propeller systems, it is common for IWVs to be equipped with multiple propellers and rudders. Typical configurations for IWVs include single-propeller twin-rudder (SPTR), twin-propeller twin-rudder (TPTR) as well as twin-propeller quadruple-rudder (TPQR) for enhanced manoeuvrability (Liu and Hekkenberg 2017).

Barges are frequently used in inland waterways due to their shallow draught (King et al. 2008) and spacious design (Koh et al. 2008). These advantages make the pusher-barge system popular across Europe, America, and Southeast Asia. In this study, the TPTR pusher-barge model in shallow water, as described in Koh and Yasukawa (2012), is employed. Their research demonstrates that

a decreased water depth results in a smaller tactical circle and adversely impacts the vessel's course-keeping ability. To analyse a vessel's trajectory under confined waterways, an accurate ship mathematical model is necessary for manoeuvring simulations. Research on ship manoeuvring models has been continuously conducted over the past decades. These models can be divided into three types: response models, whole ship models, and modular models, according to the requirements of the application. The response model, which is known as the KT model, was first proposed by Nomoto et al. (1957) as it simplifies the ship motions into a turning ability index ( $K$ ) and the course-keeping index ( $T$ ). However, this model neglects the influence of ship speed and damping force and is thus not applicable for modelling the hydrodynamic forces of inland vessels. Abkowitz (1964) proposed a whole ship model to predict the forces and movements on the ship hull in the Taylor series and proved its capability for arbitrary manoeuvring simulations. In addition, Ogawa and Kasai (1978) proposed a modular model to decompose forces and moments into individual components, the so-called Manoeuvring Modelling Group (MMG) model. One of the key advantages of the MMG model is the modular structure. The effect of each component and the interaction between them can be analysed individually. Therefore, additional factors such as shallow water and the bank effect can be easily incorporated and investigated.

This work aims to generate a rapid and accurate prediction of a vessel's motion response in confined waterways. Therefore, a manoeuvring model is developed based on the original MMG method, with modified hydrodynamic groups to capture shallow water and bank effects. The modular nature of the model allows for easy customisation to test various control strategies, control systems, environmental load effects, and applications, or integration with an energy system model (Zhang et al. 2023) to evaluate the vessel energy performance during dynamic operations. The Koh and Yasukawa pusher-barge model is selected as baseline in the study. Empirical methods for shallow water and bank-induced forces and moments are carefully examined and integrated. The model's performance is validated using free-running experimental data from turning tests at three different water depths. This work emphasises the impact of the confinement effect and compares it with the vessel's performance in infinite water conditions. Case studies demonstrate the pusher-barge system's course-keeping ability under river current and bank effects. The findings suggest that incorporating modified hydrodynamic terms can significantly enhance the applicability of the original pusher-barge model in confined waterways.

## 2. Manoeuvring group model

### 2.1. Coordinate systems

The manoeuvring simulation in this study focuses on two-dimensional (2D) planar ship motion in three degrees of freedom (DoF), i.e. surge, sway and yaw motions are considered in this study. The coordinate systems are shown in Figure 1; the vessel sails in the earth-fixed coordinate system  $o_0 - x_0y_0z_0$ , where the midship is selected as the origin of the body-fixed system  $o - xyz$ . The centre of gravity (CoG) is located at  $(x_G, 0, 0)$  in the  $o - xyz$  system, and the ship heading is represented by the angle ( $\psi$ ) between  $o_0 - x_0$  and  $o - x$ , respectively.

### 2.2. Pusher-barge profile

The study utilises the manoeuvring test data of a pusher-barge train (Koh and Yasukawa 2012), where a model-scale ( $\lambda = 50$ ) rake-barge

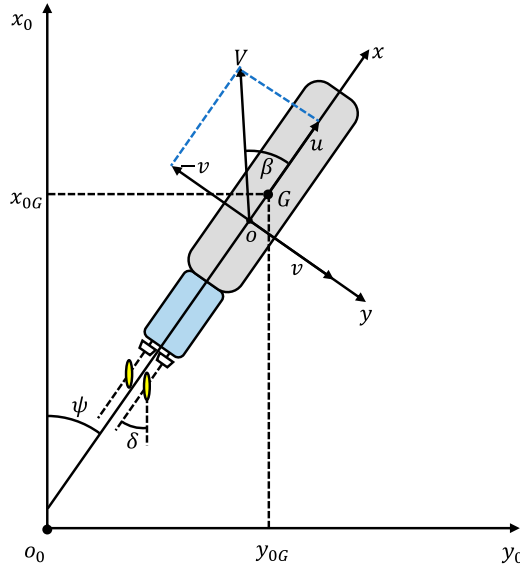


**Figure 1.** Coordinate systems in the present study. (This figure is available in colour online.)

**Table 1.** Dimensions of the pusher-barge train in full-scale (Koh and Yasukawa 2012).

Parameters	Pusher	Rake-barge	Pusher-barge train
Length, $L$ [m]	40.00	60.96	100.96
Ship Beam, $B$ [m]	9.00	10.67	10.67
Draught, $T$ [m]	2.20	2.74	2.74
Volume, $\nabla$ [m <sup>3</sup> ]	494.7	1646.2	2140.9
Block coefficient, $C_B$ [-]	0.633	0.924	0.725

**Table 2.** Dimensions of the propeller and the rudder.

Parameters	Values
Propeller diameter, $D_p$ [m]	1.8
Revolution speed, $n_p$ [rpm]	300
Rudder span, $B_R$ [m]	2.0
Rudder chord length, $C_R$ [m]	2.0
Rudder area, $A_R$ [m <sup>2</sup> ]	4.0

was connected with a pusher to formulate the 11 BP system. The dimensions of the pusher and the barge in full scale are presented in Table 1. The propellers and rudders follow a TPTR configuration; the profiles are listed in Table 2.

The hydrodynamic coefficients were derived from least squares fitting to experimental data of constant drifting and rotating arm tests under three different water depth conditions: deep water ( $H/T = 19.3$ ), medium shallow water ( $H/T = 1.5$ ), and shallow water ( $H/T = 1.2$ ). During the captive model tests, the heave, pitch, and roll motion of the pusher-barge convoy were fixed. The detailed hydrodynamic derivatives and added mass coefficients are presented in Koh and Yasukawa (2012). Based on hydrodynamic derivatives, a manoeuvring study on this 11BP system was conducted at rudder angles of 35° and 20° in calm water, where the effects of wind, wave and currents were not considered in the original tests.

### 2.3. Equations of motion

The study utilises the Manoeuvring Modelling Group (MMG) model (Ogawa and Kasai 1978) as the reference to capture the ship's motions under the interaction between external forces and moments. One of the key advantages of the MMG model is its modular-based structure, which decomposes the hydrodynamic forces

and the moments grouped into individual parts (ship hull, propeller, and rudder). However, the original MMG model is developed for conventional sea-going vessels with a single-propeller and a single-rudder, whose propeller-rudder configuration and waterway conditions differ significantly from IWVs.

Owing to the flexibility of the modular model, this study introduces a new term to represent the bank effect and to correct the hydrodynamic forces for shallow water conditions, which aims to capture the characteristics of confined inland waterways. The dynamic equations of ship motions are given as follows:

$$\left. \begin{aligned} (m + m_x)\dot{u} - (m + m_y)v_m r - x_G m r^2 &= X_H + X_P + X_R + X_B \\ (m + m_x)\dot{v}_m - (m + m_x)ur + x_G m \dot{r} &= Y_H + Y_R + Y_B \\ (I_z + x_G^2 m + J_z)\dot{r} + x_G m(\dot{v}_m + ur) &= N_H + N_R + N_B \end{aligned} \right\} \quad (1)$$

where  $m$  is the ship's mass,  $m_x$  and  $m_y$  represent the added mass in the  $x$  and  $y$ -directions,  $x_G$  is the coordinate of CoG,  $I_z$  is the moment of inertia,  $J_z$  is the added moment of inertia for yaw motion,  $X, Y, N$  denote the surge, sway forces and yaw moments, the subscripts  $H, P, R, B$  represent individual force and moment components from the ship hull, the propellers, the rudders and the bank effect, and  $u$  is the longitudinal velocity,  $v_m$  is the lateral velocity at mid-ship, and  $r$  denotes the yaw rate. The manoeuvring model is built in Matlab environment. The model setup is demonstrated in Figure 2. Formulation of individual blocks is described in subsequent sections.

### 2.4. Hydrodynamic hull forces

The hydrodynamic forces and moment acting on the ship hull are given as:

$$\left. \begin{aligned} X_H &= 0.5\rho L T U^2 X'_H \\ Y_H &= 0.5\rho L T U^2 Y'_H \\ N_H &= 0.5\rho L^2 T U^2 N'_H \end{aligned} \right\} \quad (2)$$

where  $\rho$  is the freshwater density,  $L$  is the ship length,  $T$  is the draught,  $U$  is the ship speed,  $X'_H, Y'_H, N'_H$  represent non-dimensional surge force, sway force and yaw moment, which are expressed as follows:

$$\left. \begin{aligned} X'_H &= -R'_0 \cos^2 \beta_m + X'_{\beta\beta} \beta_m^2 + X'_{\beta r} \beta_m r' + X'_{rr} r'^2 + X'_{\beta\beta\beta} \beta_m^3 \\ Y'_H &= Y'_{\beta} \beta_m + Y'_{r'} r' + Y'_{\beta\beta\beta} \beta_m^3 + Y'_{\beta\beta r} \beta_m^2 r' + Y'_{\beta r r} \beta_m r'^2 + Y'_{r r r} r'^3 \\ N'_H &= N'_{\beta} \beta_m + N'_{r'} r' + N'_{\beta\beta\beta} \beta_m^3 + N'_{\beta\beta r} \beta_m^2 r' + N'_{\beta r r} \beta_m r'^2 + N'_{r r r} r'^3 \end{aligned} \right\} \quad (3)$$

where  $R'_0$  is the non-dimensional forward resistance,  $X'_{\beta\beta}, X'_{\beta r}, \dots, N'_{r r r}$  are the hydrodynamic derivatives,  $\beta_m$  is the drift angle at mid-ship as  $\beta_m = -\tan^{-1}(v_m/u)$ ,  $r'$  is the non-dimensional yaw rate by ( $r' = rL/U$ ). To make the model applicable for inland waterways, the resistance component is corrected to include the shallow water effect; the details are presented in Zhang et al. (2023). The non-dimensional  $R'_0$  is computed by:

$$R'_0 = \frac{R_{Shallow}}{(0.5\rho L T U^2)} \quad (4)$$

where  $R_{Shallow}$  is the total resistance, including the shallow water effect, which is given as:

$$R_{Shallow} = 0.5\rho S_W U^2 (C_F(1 + (k + \Delta k)) + C_W) \quad (5)$$

where  $S_W$  is the ship's wetted surface area,  $C_F$  is the frictional resistance coefficient from the ITTC formula as  $C_F = 0.075/(\log_{10} Re - 2)^2$ ,  $Re$  is the Reynolds number,  $k$  is the



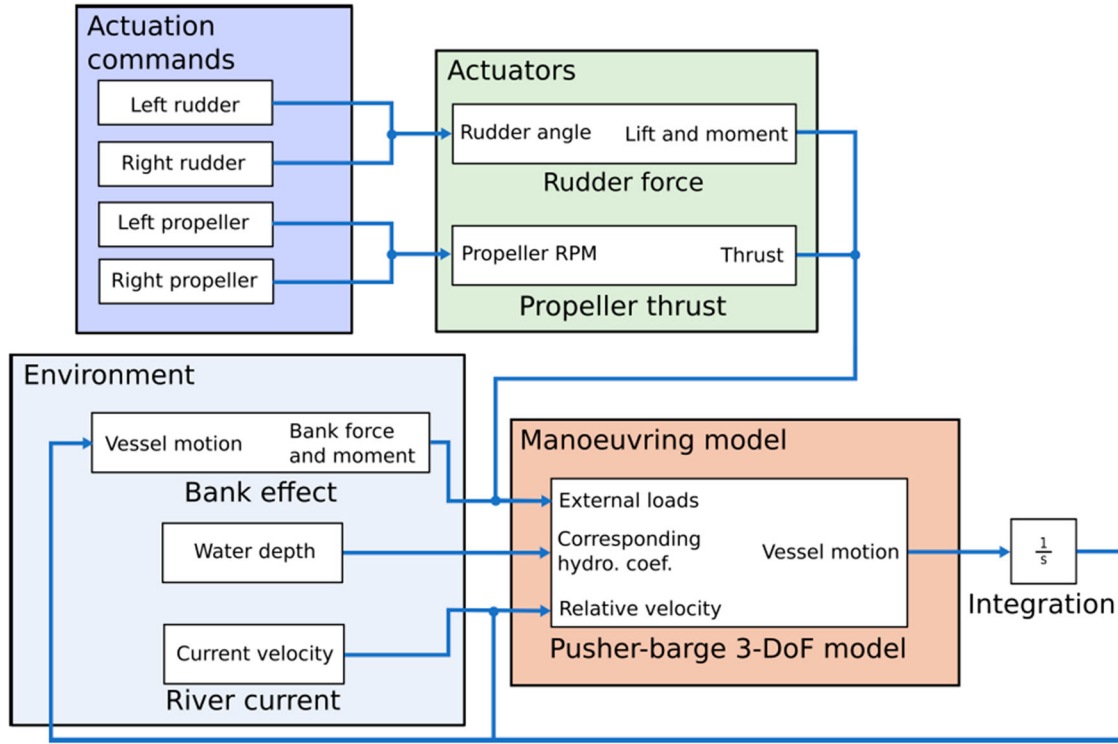


Figure 2. Confined water manoeuvring model setup. (This figure is available in colour online.)

ship's form factor in deep water,  $C_W$  is the wave-making resistance coefficient,  $\Delta k$  is the additional viscous resistance in shallow water (Millward 1989), which is computed as:

$$\Delta k = 0.644 \left( \frac{H}{T} \right)^{-1.72} \quad (6)$$

where  $H$  is the water depth. Equation (6) indicates that a decreasing water depth causes additional viscous pressure resistance on the ship hull.

## 2.5. Propeller forces

This study is conducted for a conventional twin propeller configuration, where the propeller forces are expressed as follows:

$$X_P = (1 - t)(T_P^P + T_P^S) \quad (7)$$

where  $t$  is the thrust deduction factor,  $T_P^P$  and  $T_P^S$  is the thrust from the propeller in portside and starboard, respectively, given as:

$$T_P^P = T_P^S = \rho n_p^2 D_p^4 K_T \quad (8)$$

where  $n_p$  is the propeller speed,  $D_p$  is the propeller diameter,  $K_T$  is the thrust coefficient, given as:

$$K_T = k_2 J^2 + k_1 J + k_0 \quad (9)$$

where  $J$  is the advance ratio of the propeller, defined as:

$$J = u(1 - w_p)/(n_p D_p) \quad (10)$$

where  $u$  is the ship surge velocity,  $w_p$  is the wake fraction during steering and is defined as:

$$w_p/w_{p0} = \exp(-4\beta_p^2) \quad (11)$$

where  $w_{p0}$  is the wake fraction during straight moving,  $\beta_p$  is the

inflow angle to the propeller during steering, which is computed by  $\beta_p = \beta - (x_p/L)r'$  where  $x_p$  is the longitudinal coordinates of the propeller.

It is noticed that  $t$  and  $w_{p0}$  are assumed to be identical for each propeller, for model simplification. Analysing the unsymmetrical inflow for twin propellers during steering is complicated, requiring model test or high-fidelity CFD simulation and is thus out of scope in this study.

## 2.6. Forces and moment on the rudders

The forces and the moment acting on the rudders are expressed by:

$$\left. \begin{aligned} X_R &= -(1 - t_R)(F_N^P + F_N^S) \sin \delta \\ Y_R &= -(1 + \alpha_H)(F_N^P + F_N^S) \cos \delta \\ N_R &= -(x_R + \alpha_H x_H)(F_N^P + F_N^S) \cos \delta \end{aligned} \right\} \quad (12)$$

where  $F_N$  is the rudder normal force,  $t_R$  is the steering resistance deduction factor,  $\alpha_H$  is the rudder force increase factor,  $x_R$  is the longitudinal coordinate of rudders and it is identical for the portside and starboard,  $x_H$  is the longitudinal coordinate of the acting point of the additional lateral force, and  $\delta$  is the rudder angle. The  $F_N$  is defined as:

$$F_N = 0.5 \rho A_R U_R^2 C_N \quad (13)$$

where  $A_R$  is the rudder area,  $U_R$  is the flow velocity at the rudder ( $U_R = \sqrt{u_R^2 + v_R^2}$ ),  $C_N$  is the rudder normal force coefficient, which can be computed as:

$$C_N = \frac{6.13\Lambda}{\Lambda + 2.25} \sin \alpha_R \quad (14)$$

where  $\Lambda$  is the rudder aspect ratio as  $\Lambda = B_R/C_R$  (where  $B_R$  is the rudder span and  $C_R$  is the chord length, respectively),  $\alpha_R$  is the

effective inflow angle at the rudder, which is given as:

$$\alpha_R = \delta - \tan^{-1}\left(\frac{v_R}{u_R}\right) \quad (15)$$

The longitudinal rudder inflow speed  $u_R$  and the lateral rudder inflow speed  $v_R$  are defined as:

$$u_R = \frac{\varepsilon u_P}{1-s} \sqrt{1 - 2(1-\eta\kappa)s + \{1-\eta\kappa(2-\kappa)\}s^2} \quad (16)$$

where  $\gamma_R$  is the flow straightening coefficient,  $l'_R$  is an experimental constant for the acting point of  $v_R$  from a captive model test,  $\varepsilon$  is the ratio of wake fraction at the rudder to the propeller as  $\varepsilon = (1-w_R)/(1-w_P)$ ,  $s$  is the propeller slip ratio,  $\eta$  is the propeller diameter and rudder span relative ratio as  $\eta = D_P/B_R$ , and  $\kappa$  is an experimental constant for  $u_R$ .

## 2.7. Bank effect

During daily operations, inland vessels will inevitably encounter confined waterways, such as narrow rivers, canals, or locks. When the ship approximates the bank, the channel wall generates additional hydrodynamic forces and moments in the vicinity of the hull. The ship can suffer from increased resistance and a bow-out moment, the so-called bank effect. To include these in the model and to be able to simulate these phenomena, a new term caused by the bank effect is introduced to the original MMG model. The additional forces and moment are computed using the empirical formulas from Vantorre et al. (2003), which are given as:

$$\begin{aligned} Y_B &= Y_B^H + Y_B^P + Y_B^{HP} \\ N_B &= N_B^H + N_B^P + N_B^{HP} \end{aligned} \quad (17)$$

where the superscripts  $H$ ,  $P$ ,  $HP$  represent the effects of forward speed (ship hull), propulsions and coupled effect between speed and propulsion, which are defined as:

$$\left. \begin{aligned} Y_B^H &= 0.5\rho L T u^2 \sum_{i=1}^2 \sum_{k=0}^2 \alpha_{ik}^H y_B^i \left(\frac{T}{H-T}\right)^k \\ N_B^H &= 0.5\rho L^2 T u^2 \sum_{i=1}^2 \sum_{k=0}^2 \beta_{ik}^H y_B^i \left(\frac{T}{H-T}\right)^k \\ Y_B^P &= 0.5\rho L T V_T^2 \sum_{i=1}^2 \sum_{k=0}^2 \alpha_{ik}^P y_B^i \left(\frac{T}{H-T}\right)^k \\ N_B^P &= 0.5\rho L^2 T V_T^2 \sum_{i=1}^2 \sum_{k=0}^2 \beta_{ik}^P y_B^i \left(\frac{T}{H-T}\right)^k \\ Y_B^{HP} &= 0.5\rho L T V_T^2 Fr \sum_{i=1}^2 \sum_{k=0}^2 \alpha_{ik}^{HP} y_B^i \left(\frac{T}{H-T}\right)^k \\ N_B^{HP} &= 0.5\rho L^2 T V_T^2 Fr \sum_{i=1}^2 \sum_{k=0}^2 \beta_{ik}^{HP} y_B^i \left(\frac{T}{H-T}\right)^k \end{aligned} \right\} \quad (18)$$

where  $V_T$  is the reference velocity,  $Fr$  is the Froude number,  $\alpha_{ik}^H$ ,  $\beta_{ik}^H$ ,  $\alpha_{ik}^P$ ,  $\beta_{ik}^P$ ,  $\alpha_{ik}^{HP}$ ,  $\beta_{ik}^{HP}$  are coefficients from regression analysis (see Appendix A for details), and  $y_B$  is the non-dimensional ship-bank distance, given as:

$$y_B = \frac{1}{2}B\left(\frac{1}{y_p} + \frac{1}{y_s}\right) \quad (19)$$

where  $y_p$  is the distance of ship to portside bank, and  $y_s$  is the distance of midship to bank in starboard.

It should be noted that the original method neglects the longitudinal forces ( $X_B \approx 0$ ); however, a series of research studies

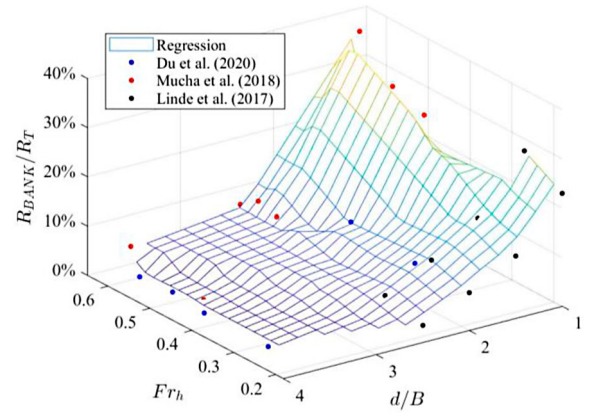


Figure 3. Regression surface for bank-induced resistance (Zhang et al. 2023). (This figure is available in colour online.)

(Zou and Larsson 2013; Lataire 2014; Mucha et al. 2018) found that the bank effect significantly impacts the resistance if the ship sails close enough to the bank. Therefore, this study utilises the method from Zhang et al. (2023) to calculate the additional resistance due to the bank effect based on ship-bank distance  $d$  and depth Froude number  $Fr_h$  (i.e. the relationship between the ship's speed and the water depth); the regression surface is shown in Figure 3.

## 2.8. Model limitations and applicability

The abovementioned manoeuvring model focuses on motion predictions for inland vessels with conventional twin-propeller and twin or multiple rudder configurations. The model is not applicable to other types of steering systems, such as azimuth thrusters. Due to the complexity of analysing the flow interactions between the propellers and multiple rudders, it is assumed that the propeller thrust is identical on both sides, and each rudder is considered to generate the same steering force, meaning that the effect of asymmetrical flow is neglected.

All forces and moments are considered acting at the CoG. The rudder angle limit ranges from  $-45^\circ$  to  $45^\circ$ , and the incoming flow angle is identical for every rudder during manoeuvring. Regarding the bank effect, the mathematical model applies to straight channel navigation, according to experiments in the literature. This implies that the hydrodynamic effects at curved fairways, such as river bends, cannot be validated with the current method.

## 3. Results and discussion

### 3.1. Model verification study

The manoeuvring model is verified using the hydrodynamic derivatives from Koh and Yasukawa (2012), see Appendix B for the vessels' parameters, where turning tests were conducted under two rudder angles:  $\delta = 35^\circ$  and  $\delta = 20^\circ$  at a speed of  $U = 0.364$  m/s (5 knots in full-scale); it should be noticed that the fourth-order derivative  $X'_{\beta\beta\beta\beta}$  was neglected in their original study. The comparison of the proposed model's simulation results and the data in the literature are shown in Figures 4 and 5. The overall results agree with the reference data. The comparison of tactical diameters and advance distances are summarised in Figures 6 and 7, the results showcase that the developed manoeuvring model can capture the motion of TPTR ships for different rudder angles. Nevertheless, it is also noticed that there are some deviations between the simulation results and the measured data, especially for the water

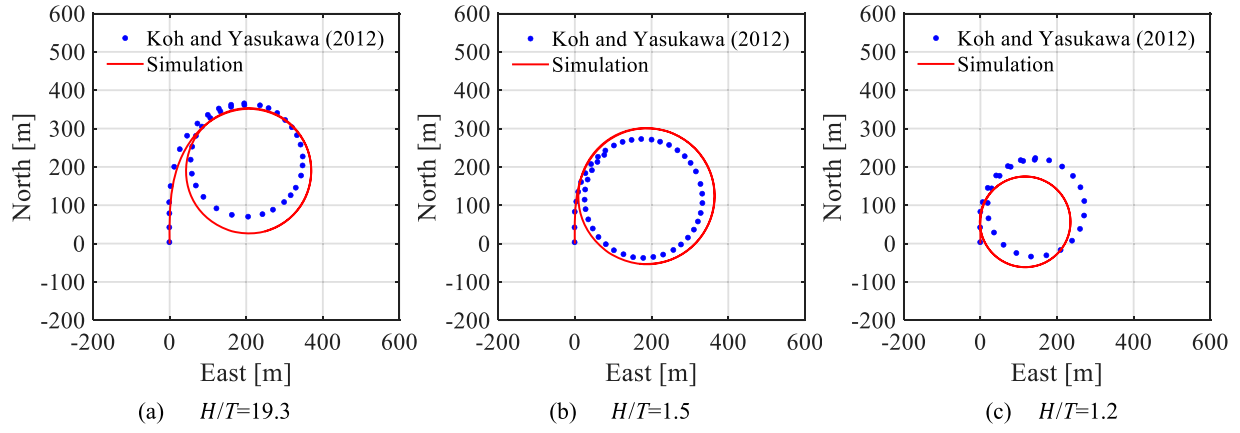


**Figure 4.** Model verification for free running test ( $\delta = 35^\circ$ ): (a)  $H/T = 19.3$  (b)  $H/T = 1.5$  (c)  $H/T = 1.2$ . (This figure is available in colour online.)

depth of  $H/T = 1.5$  under both rudder angles, which are shown in Figures 4 and 5(b). This might be due to an underestimation of the rudders' normal force coefficient by the empirical formula, resulting in smaller rudder moments for the different tactical diameters. Besides, since some parameters are missing in the literature, the vessel's CoG (4.5 m to midship) and relative position of propellers ( $-47.5$  m) and rudders ( $-50.0$  m) are estimated by the authors, which can also contribute to some discrepancies from the original vessel's trajectory. The verification study shows that the manoeuvring model accurately predicts the vessel's motion.

### 3.2. Sensitivity study on hydrodynamic derivatives

A sensitivity study was performed using the indirect method to analyse the impact of individual hydrodynamic derivatives. The sensitivity value was calculated by varying each coefficient for a certain amount, recording the relative change of model output during every simulation, and iterating until all the parameters are evaluated (Yeo and Rhee 2006). The normalised sensitivity value is defined as:

$$S_i = \frac{\theta_i}{y} \frac{\partial y}{\partial \theta_i} \approx \frac{\theta_i}{y} \frac{y(\theta_i + \Delta\theta_i) - y(\theta_i)}{\Delta\theta_i} \quad (20)$$

where  $S_i$  is the normalised sensitivity value,  $y$  is the model output (tactical diameter),  $\theta_i$  represents the value of  $i$ th parameter.  $\Delta\theta_i$  is the small amount of parameter change, which is 10% in this study.

The simulations were conducted at the same rudder angles in Section 3.1, and the results are presented in Figure 8. It shows that the linear terms have the most significant impact on the vessel's trajectory. Nevertheless, with an increasing rudder angle, the influence of non-linear terms, such as  $N_{\beta\beta\beta}$ ,  $N_{\beta\beta r}$ , and  $N_{\beta rr}$ , become noticeable when the vessel is executing tight manoeuvres. In European waterways, inland vessels nowadays are expected to use rudders allowing maximum rudder angles of up to 90 degrees, which means that special attention should be paid to the regression analysis of these non-linear hydrodynamic derivatives when conducting manoeuvring tests.

### 3.3. Simulation of bank effect

The simulation of the bank effect was conducted in a straight channel under different starboard-bank distances  $y_s$ . The aim was to analyse the effect of bank-induced forces and moments on the ship's trajectory and thus investigate the applicability of the manoeuvring model in confined inland waterways. It should be noticed that the vessel was assumed to sail at a rudder angle of  $0^\circ$ ; thus, the simulations were focused purely on the bank effect on ship motions. The channel has a rectangular cross-section with a width ( $W_C$ ) of 100 m, and the vessel sails at an initial speed of 5 knots and 0 heading with acting propellers of 150 rpm. It is noted that a non-dimensional value  $y'_s$  is used

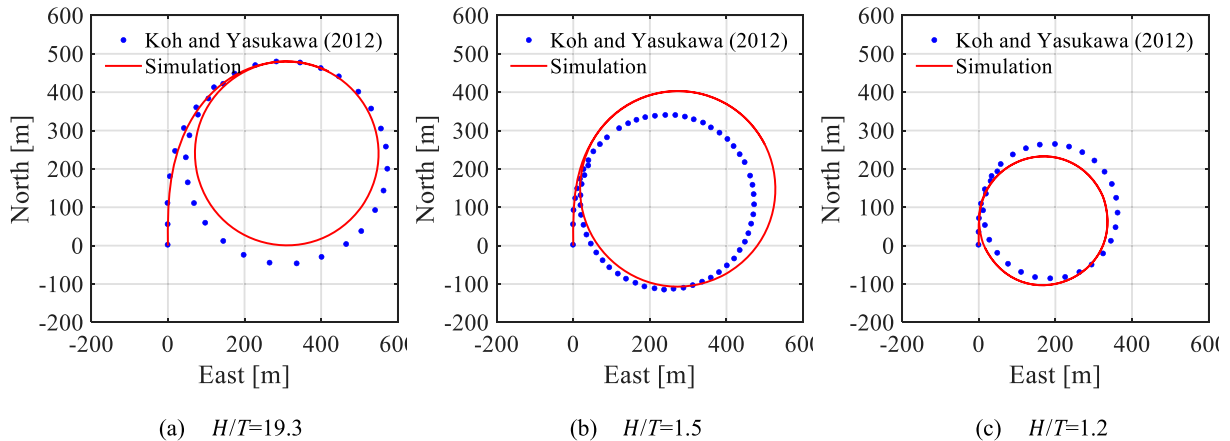


**Figure 5.** Model verification for the free running test ( $\delta = 20^\circ$ ): (a)  $H/T = 19.3$  (b)  $H/T = 1.5$  (c)  $H/T = 1.2$ . (This figure is available in colour online.)



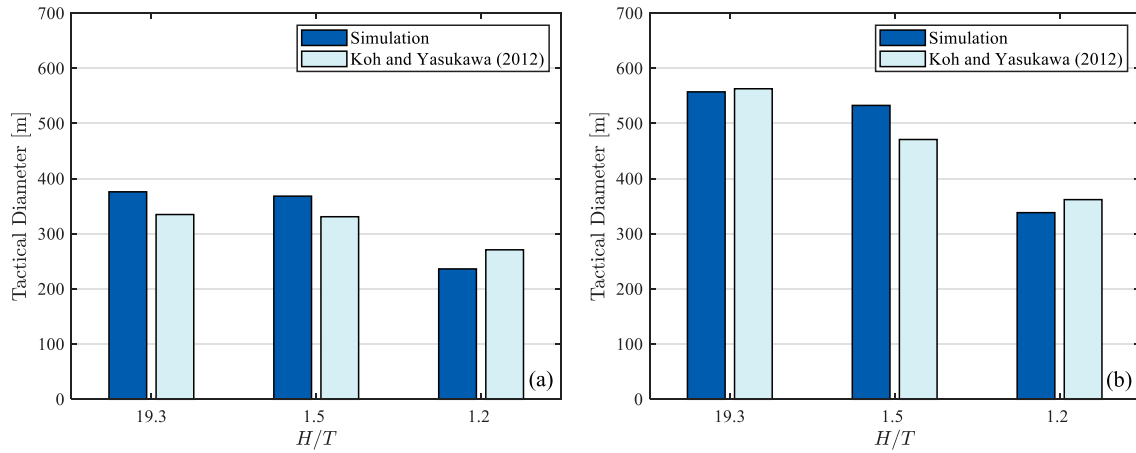


Figure 6. Comparison of tactical diameters at each rudder angle: (a)  $\delta = 35^\circ$  and (b)  $\delta = 20^\circ$ . (This figure is available in colour online.)

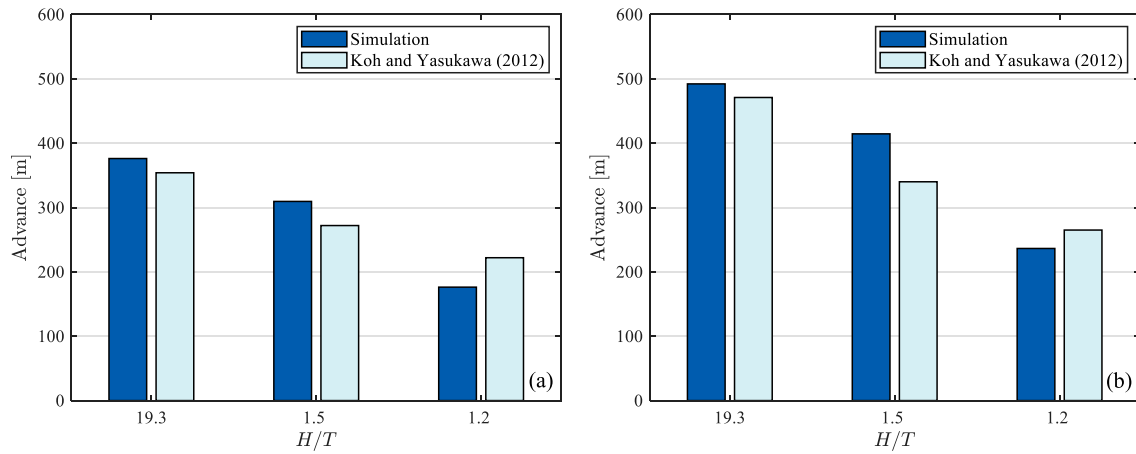


Figure 7. Comparison of advance distances at each rudder angle: (a)  $\delta = 35^\circ$  and (b)  $\delta = 20^\circ$ . (This figure is available in colour online.)

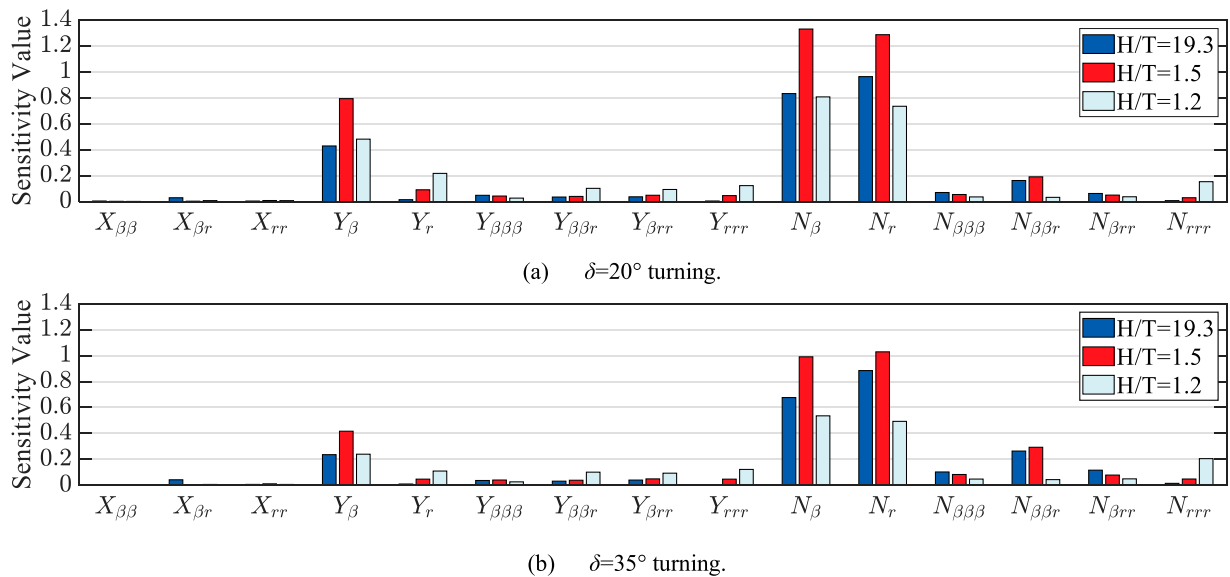
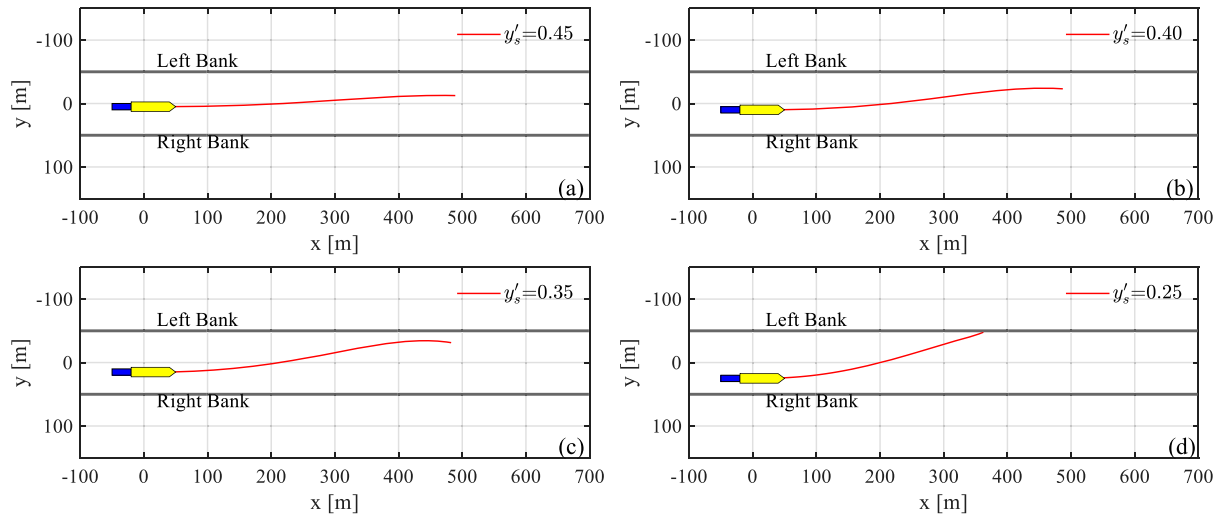


Figure 8. Sensitivity analysis on the hydrodynamic derivatives.: (a)  $\delta = 20^\circ$  turning, (b)  $\delta = 35^\circ$  turning. (This figure is available in colour online.)



**Figure 9.** Vessel trajectories under different  $y'_s$  ( $H/T = 19.3$ ), the initial vessel speed is 5 knots with propeller rate of 150 rpm. (This figure is available in colour online.)

here to represent the ratio of ship-bank distance to the channel width ( $y'_s = y_s/W_C$ ).

Figure 9 shows the vessel's position under various initial  $y_s$  in deep water ( $H/T = 19.3$ ), the simulation time was set to 200 s for all the cases. It is found that the channel wall has limited impact on the vessel's motion when it sails relatively close to the channel centre ( $y'_s = 0.5$ ). First, the ship turns slightly to the portside and then follows the centre line, as shown in Figure 9(a). Once the ship comes closer to the riverbank, the decreased  $y'_s$  contributes to stronger hydrodynamic forces acting on the hull. This results in a deviation from the predefined heading, as shown in Figure 9 (b and c). The vessel turns towards the left bank first, and once it passes the centre line, the bank on the other side generates moments but in the opposite direction, which alters the ship's heading and deviates around the middle channel. This is due to the pressure difference between each side of the vessel. When the ship's starboard is close to the channel wall, the flow speed on this side accelerates, thus contributing to lower pressure than on the port side. Such pressure difference causes suction forces towards the bank, and the force at the stern is larger than the bow because of flow acceleration near the acting propeller. Therefore, the ship suffers from a yaw moment, the so-called bow-out moment (Vantorre et al. 2003). When the ship-bank distance keeps decreasing, as shown in Figure 9(d), it can be found from the trajectory that the ship is exposed to a strong bow-out moment and keeps swinging towards the left bank and colliding on it.

The effect of water depth is shown in Figure 10. The simulation was conducted at three different water depths. When the vessel was sailing close to the middle channel ( $y'_s = 0.45$ ), it is subject to

a more significant bank effect under the decreasing water depth. Especially at the minimum water depth condition ( $H/T = 1.2$ ), the vessel has an obvious risk of colliding with the right bank after turning back from the other side of the channel. When the vessel sails closer to the right bank, as shown in Figure 10(b), it should be carefully noted that shallow water intensifies the bank effect under a shorter ship-bank distance. The vessel can directly crush on the left bank under lower under-keel clearance (UKC) if there is no rudder action. This phenomenon can be explained by Equation (18), where a smaller UKC ( $H - T$ ) will increase the forces and bow-out moments induced by the channel bank, making ship manoeuvre on narrow fairways challenging under the given propeller rpm.

An additional simulation was conducted under four sets of rpm to investigate further the effect of propeller speeds on these bank-induced forces and moments. Figure 11 shows the vessel trajectories under two water depths, and it is evident that the vessel is likely to suffer from the risk of collision at higher speeds, especially when the water is shallow, as shown in Figure 11(b). This means a careful rudder execution needs to be performed to maintain the course, and high-speed sailing must be avoided to ensure operational safety, as indicated in Vantorre et al. (2017).

### 3.4. Rudder action for course-keeping under currents

Considering the significant influence of the bank effect on ship motions on confined waterways, simulations of rudder control were conducted to investigate the rudder action for course-keeping. A Proportional-Derivative (PD) controller was incorporated into the manoeuvring simulation to adjust the

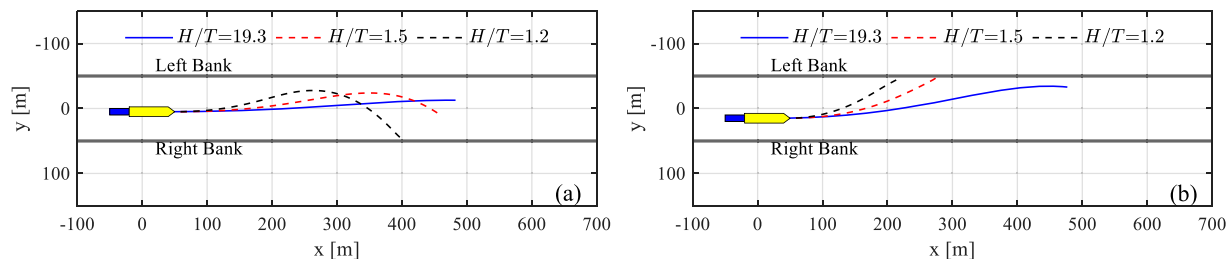


**Figure 10.** Bank effect under different water depths: (a)  $y'_s = 0.45$  and (b)  $y'_s = 0.35$ . (This figure is available in colour online.)

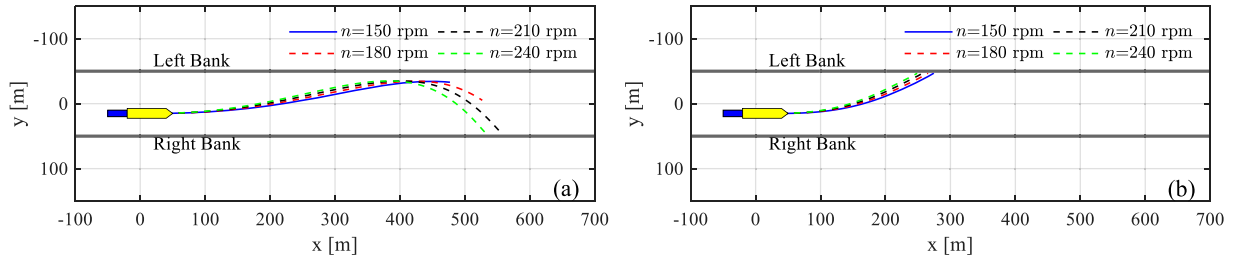


**Figure 11.** Coupled bank effect with various propeller speeds,  $y'_s = 0.35$ : (a)  $H/T = 19.3$  and (b)  $H/T = 1.5$ . (This figure is available in colour online.)

rudder angle, represented by:

$$\delta_C = -K_P \left( (\psi - \psi_{Ref}) + T_D \frac{d(\psi - \psi_{Ref})}{dt} \right) \quad (21)$$

where  $\delta_C$  is the command rudder angle,  $K_P$  is the controller P-gain,  $T_D$  is the controller derivative time and  $\psi_{Ref}$  is the desired heading, which is defined by:

$$\psi_{Ref} = \begin{cases} 0 & (\text{Mid-channel}) \\ \tan^{-1} \left( \frac{\Delta y}{X_D} \right) & (\text{Sailing along banks}) \end{cases} \quad (22)$$

In Equation (22), it means that if the target course is in mid-channel, the ship will take a zero-heading angle as the reference, and the rudder will adjust it accordingly to steer the vessel to sail in the waterway centre, where the bank effects are counteracted. Furthermore, this operational scenario is essential for the vessel's course stability under very narrow and shallow fairways. The other operational condition is sailing along riverbanks; it requires the vessel to maintain a relatively constant lateral distance to the shore to ensure safety when encountering other vessels during head-on or overtaking. Therefore,  $\Delta y$  is the difference between the current lateral position ( $y(t)$ ) and the desired lateral position ( $y_{ini}$ ), which is defined as  $\Delta y = y_{ini} - y(t)$ , and  $X_D$  is a predefined length to represent the triangle (80 m used in this study). It means that if the desired position is at the starboard side of the vessel ( $y_{ini} > y(t)$ ), the controller will adjust the rudder angle to have a positive heading for the target course, and vice versa if it is at the portside to the ship; an illustration is shown in Figure 12. This situation is challenging to the rudder execution as the vessel can be exposed to strong bank effects on confined waterways.

The simulations in this section were all conducted at a relatively shallow water level (where  $H/T = 1.5$ ). To fulfil the general operational conditions for inland vessels, the coupled effect of river current was also introduced, where the maximum current speed was set to 0.5 m/s. According to Fossen (2011), the relative ship speed

for manoeuvring facing river current can be computed by:

$$\begin{aligned} u_r &= u - U_C \cos(\beta_C - \psi) \\ v_r &= v - U_C \sin(\beta_C - \psi) \end{aligned} \quad (23)$$

where the angle of the incoming current ( $\beta_C$ ) is  $180^\circ$  when the ship is sailing upstream and  $0^\circ$  for downstream sailing, respectively.

### 3.4.1. Rudder control for mid-channel sailing

To set a vessel on course and ensure its navigation in the mid-channel, a desired heading of  $0^\circ$  was established. This implies that the controller's objective is to adjust the rudder angle, allowing the ship to travel in a straight line while compensating for the effects of the riverbanks. Figure 13 shows the vessel trajectories within a simulation time of 1200 s for different current directions.

It can be observed from the vessel's trajectory that during upstream navigation, the vessel maintains a relatively stable course, gradually approaching the centreline of the waterway. In contrast, the vessel encounters challenges when manoeuvring against the downstream current, as shown in Figure 13(b), it crosses the mid-channel at first, following a zigzag path until it aligns with the target course. In addition, the time histories of rudder action and corresponding heading angles are shown in Figure 14. It is worth noting that, under downstream current, the vessel might suffer from insufficient rudder inflow speed compared to upstream navigation. This results in an increase in the rudder angle to generate additional side forces and moments, thereby compensating for external hydrodynamic loads (as indicated by the red dashed line). Overall, the designed PD controller effectively regulates the rudder in response to the vessel's state, ensuring that the course aligns with the mid-channel. Consequently, the vessel maintains a heading angle of  $0^\circ$  in both directions, as shown in Figure 14(b).

### 3.4.2. Rudder control for sailing along riverbanks

To ensure the operational safety of inland vessels within confined waterways, it is commonly recommended that the vessel should

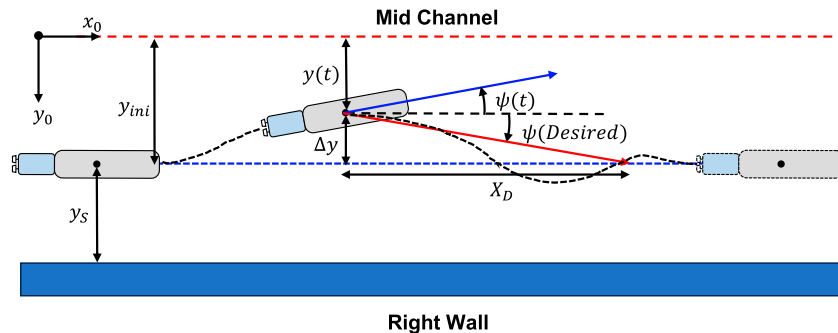


**Figure 12.** Illustration of heading control. (This figure is available in colour online.)

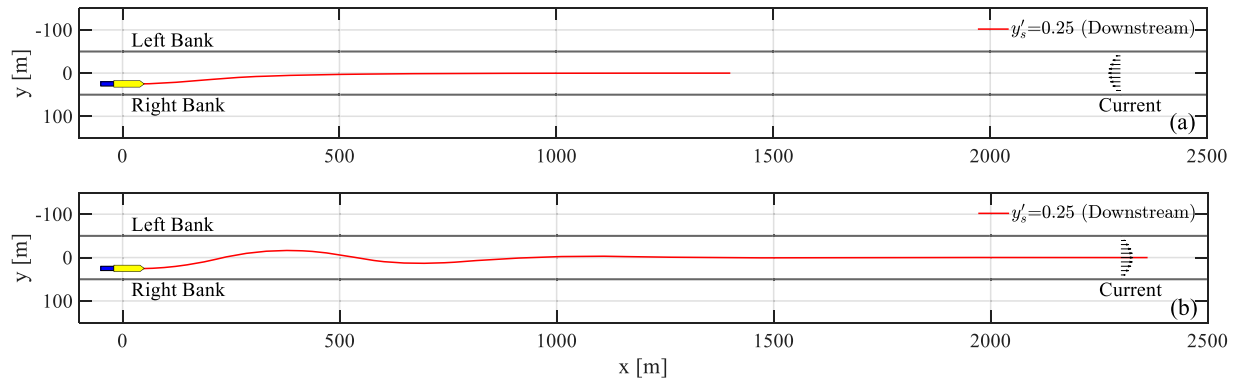


Figure 13. Vessel trajectories when sailing along right bank with rudder control,  $n = 100$  rpm. (This figure is available in colour online.)

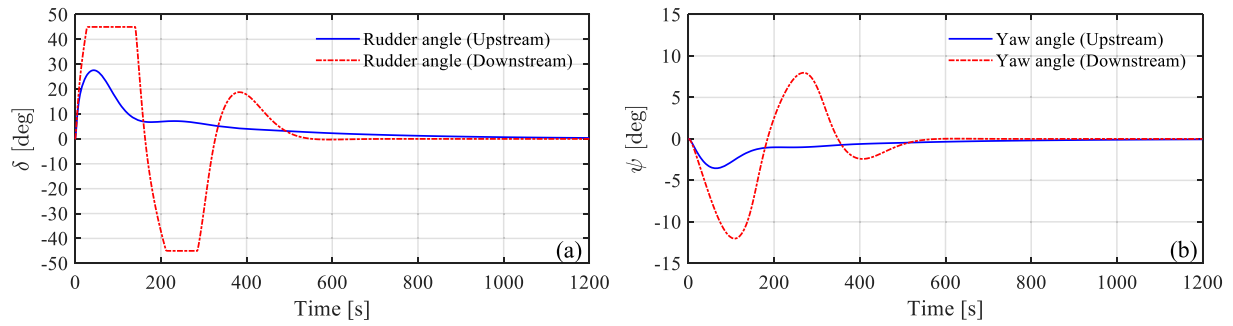


Figure 14. Time histories of the rudder and heading angles for different current directions. (This figure is available in colour online.)

reduce its speed to mitigate the risk of squat or bank effect. Therefore, it is assumed that the vessel sails at a relatively low propeller speed ( $n = 100$  rpm) for simulating the vessel's operations along riverbanks.

Figure 15 shows the vessel trajectory proceeding upstream with rudder action during a simulation time of 1200 s. It is worth noticing that at the beginning, the vessel is subject to a yaw moment and turning towards the left bank. With a rudder adjustment, the ship then gradually returns to the predetermined track and maintains its course instead of passing through the middle channel. The result indicates that the PD controller can tune the rudder angle effectively to compensate for the bank-induced moments and keep the

vessel's course at the predefined  $y_s$ . The time histories of the side forces, rudder angle  $\delta$  and the heading angle  $\psi$  are presented sequentially in Figure 15(b–d). The result shows that, with the assistance of rudder control, the ship can eventually sail on a straight course where the lateral forces are in equilibrium, and the rudder angle and heading converge to a steady state under rudder execution.

Figure 16 shows the trajectory under the downstream current. It is evident that the vessel is unable to stabilise its course and continues to oscillate around the desired path. Given that the vessel was originally equipped with twin rudders (TPTR configuration), it is likely that the reduced inflow speed at the rudder during

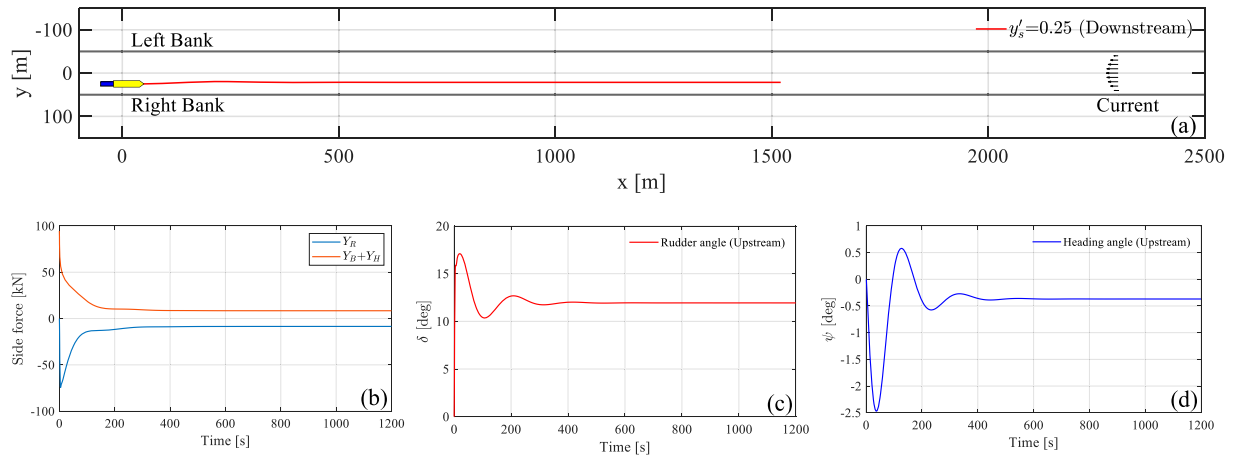


Figure 15. Vessel trajectory and time histories of rudder control for upstream sailing close to the right bank. (This figure is available in colour online.)

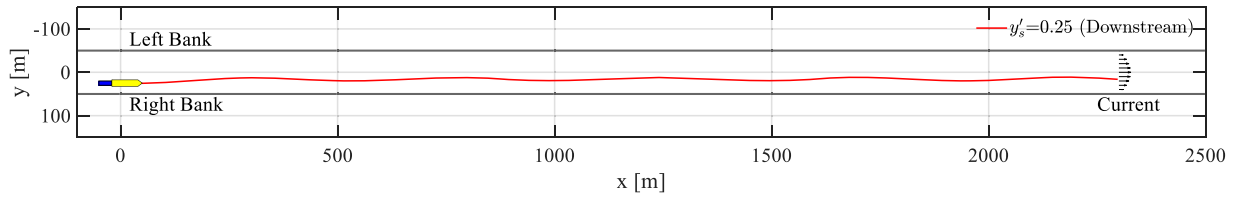


Figure 16. Vessel trajectory for downstream sailing, the vessel is equipped with twin rudders. (This figure is available in colour online.)

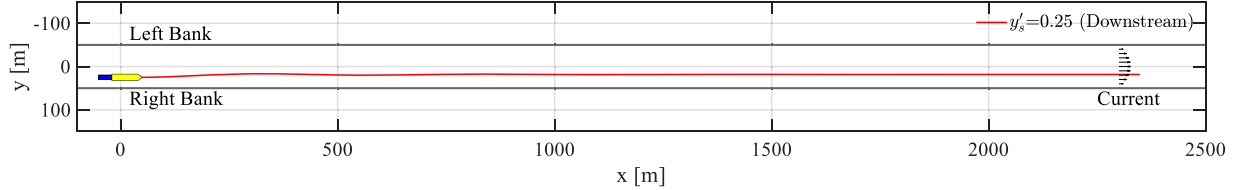


Figure 17. Vessel trajectory for downstream sailing, the vessel is refined with TPQR configuration. (This figure is available in colour online.)

downstream navigation might lead to insufficient rudder nominal force, especially when the vessel operates at a low propeller speed. This results in the rudder control not converging and the vessel presenting an unstable trajectory along the bank.

Therefore, this study further investigated the impact of the number of rudders on the controller's performance. In contrast to the TPTR system, the vessel was updated by equipping four rudders (TPQR) for better manoeuvrability, and the simulation result is presented in Figure 17. From the vessel's trajectory, it is important to notice that the TPQR configuration can successfully adjust the vessel's heading to stabilise its course to align with the target. The time histories of rudder action are showcased in Figure 18, which shows that the rudder is struggling with insufficient load under TPTR configuration, and the rudder angle keeps oscillating around a very wide range (Figure 18(a)), while in contrast, the rudder shows fairly good result and converging as expected if the vessel uses a TPQR system, as shown in Figure 18(b).

The simulations above can give insights into how the current may significantly impact the behaviour of vessels operating on confined inland waterways during low-speed operations. Sufficient rudder forces are critical for course stabilisation and operational safety, especially for vessels with twin-rudder configuration. In addition, though contemporary inland vessels are equipped with

advanced propulsion and steering units, additional attention should be considered during navigation on narrow channels when proceeding head-on and overtaking with other vessels as they might have an additional impact on the hydrodynamic forces. However, the current simulation only considers operations of a single vessel; cases of multiple vessel operations are out of the scope of the present study. Ship-ship interaction will be discussed in future work, as they are very common scenarios during the daily operations on inland waterways.

Generally, the developed manoeuvring model can give a fast (short simulation time) prediction of vessel motions under confined waterways. However, there are some limitations to be addressed in future studies. First, only a rectangular fairway cross-section was considered, where the slope and arbitrary shape of the channel wall should be investigated. Second, the channel was assumed to be straight in this study. Curved-shaped fairways or river intersections with current fields should be investigated in future work to better capture the actual inland waterway conditions and study the vessel's steering performance under these conditions. Finally, the manoeuvring model will be incorporated with the energy system model presented in Zhang et al. (2023) and routing algorithms to investigate energy consumption under long-term vessel operation conditions.

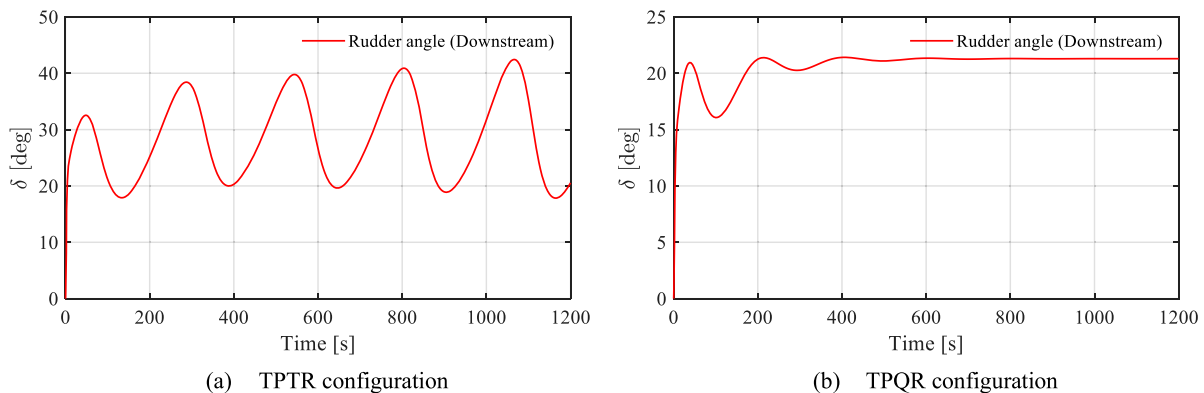


Figure 18. Time histories of rudder control for different rudder configurations.: (a)TPTR configuration (b) TPQR configuration. (This figure is available in colour online.)



## 4. Conclusions

This study presented the development of a manoeuvring model for IWV to predict ship motions in inland waterways. The mathematical model was built on the original MMG model for conventional commercial vessels. To make the model applicable to the generic operational conditions of IWVs, shallow water and bank effects were included for modelling the hydrodynamic impact of confined waterways on ship hulls.

Results of the manoeuvring study of a pusher-barge system were utilised to verify the model. The 35° and 20° turning results agree well with the literature data. It was found that the proposed model was verified and could capture the hydrodynamic characteristics of the pusher-barge convoy. The model will be investigated across various vessel types in future studies based on available experimental measurements. This aims to test the model's applicability to generic inland vessels with different propulsion units, such as azimuth thrusters and tunnel thrusters.

Extended simulations of the influence of the bank effect were conducted for various starboard-bank distances  $y_s$ . The ship trajectories showed noticeable yaw motion caused by the bank effect if the vessel was close to the channel wall. This is an essential capability of the developed model. It was also found that the increased hydrodynamic forces on the ship hull under extreme shallow water conditions will suppress the ship's motion.

Case studies for rudder control were presented to analyse the rudder action for course keeping under the dynamic coupled effects of bank force and river currents. The results showed the capability of the PD controller to steer the vessel to counteract the bank effect and maintain the predefined course. The vessel can steer against the coupled bank and current effect by utilising the rudder control to maintain its course. This simulation case is an auspicious example that can be extended to investigate more complex scenarios in future studies, such as dock operation, bridge pass, and multi-vessel interaction (head-on and overtaking, etc.). However, this study only considered rectangular fairway cross-sections. Thus, arbitrary sloped banks, including bathymetry data, will be included in future work to further improve the model's applicability to generic inland waterways.

## Acknowledgements

This project has received funding from the European Union's EU Framework Programme for Research and Innovation Horizon 2020 under Grant Agreement No. 955768 (ETN AUTOBarge). Project website: <https://etn-autobarge.eu/>.

## Data availability statement

The authors confirm that the data supporting the findings of this study are available within the article.

## Disclosure statement

No potential conflict of interest was reported by the author(s).

## Funding

This project has received funding from the European Union's EU Framework Programme for Research and Innovation Horizon 2020 under grant Agreement No. 955768 (ETN AUTOBarge).

## ORCID

Chengqian Zhang  <http://orcid.org/0009-0005-5329-6655>

## References

- Abkowitz MA. 1964. Lectures on ship hydrodynamics—Steering and manoeuvrability.
- Christodoulou A, Christidis P, Bisselink B. 2020. Forecasting the impacts of climate change on inland waterways. *Transportation Research Part D: Transport and Environment*. 82:102159. doi:10.1016/j.trd.2019.10.012.
- European Commission. 2023. Promotion of inland waterway transport [accessed 2023 Nov 18]. [https://transport.ec.europa.eu/transport-modes/inland-waterways/promotion-inland-waterway-transport\\_en](https://transport.ec.europa.eu/transport-modes/inland-waterways/promotion-inland-waterway-transport_en).
- Eurostat. 2022. 77% of inland freight transported by road in 2020 [accessed 2023 Nov 18]. <https://ec.europa.eu/eurostat/web/products-eurostat-news/-/ddn-20220425-2>.
- Fossen TI. 2011. Handbook of marine craft hydrodynamics and motion control. United Kingdom: John Wiley & Sons.
- Hansson J, Månsson S, Brynolf S, Grahm M. 2019. Alternative marine fuels: prospects based on multi-criteria decision analysis involving Swedish stakeholders. *Biomass Bioenergy*. 126:159–173.
- Hofman M, Kozarski V. 2000. Shallow water resistance charts for preliminary vessel design. *Int Shipbuilding Prog*. 47:61–76.
- Jachowski J. 2008. Assessment of ship squat in shallow water using CFD. *Arch Civil Mech Eng*. 8:27–36. doi:10.1016/S1644-9665(12)60264-7.
- Kim D, Tezdogan T, Incecik A. 2022. Hydrodynamic analysis of ship manoeuvrability in shallow water using high-fidelity URANS computations. *Appl Ocean Res*. 123:103176. doi:10.1016/j.apor.2022.103176.
- King KK, Yasukawa H, Hirata N, Kose K. 2008. Maneuvering simulations of pusher-barge systems. *J Mar Sci Technol*. 13:117–126. doi:10.1007/s00773-007-0267-4.
- Koh KK, Yasukawa H. 2012. Comparison study of a pusher-barge system in shallow water, medium shallow water and deep water conditions. *Ocean Eng*. 46:9–17. doi:10.1016/j.oceaneng.2012.03.002.
- Koh KK, Yasukawa H, Hirata N. 2008. Hydrodynamic derivatives investigation of unconventionally arranged pusher-barge systems. *J Mar Sci Technol*. 13:256–268. doi:10.1007/s00773-008-0004-7.
- Landsburg AC, Barr RA, Daggett L, Hwang W-Y, Jakobsen B, Morris M, Vest L. 2005. Critical needs for ship maneuverability: lessons from the houston ship channel full-scale maneuvering trials. *Mar Technol SNAME News*. 42:11–20. doi:10.5957/mtl.2005.42.1.11.
- Lataire E. 2014. Experiment based mathematical modelling of ship-bank interaction Ghent University.
- Liu J, Hekkenberg R. 2017. Sixty years of research on ship rudders: effects of design choices on rudder performance. *Ships Offsh Struct*. 12:495–512. May 19. doi:10.1080/17445302.2016.1178205.
- Liu J, Hekkenberg R, Rotteveel E. 2014. A proposal for standard manoeuvres and parameters for the evaluation of inland ship manoeuvrability. *Proceedings of the European Inland Waterway Navigation Conference*, 2014, Budapest, Hungary.
- Liu J, Hekkenberg R, Rotteveel E, Hopman H. 2015. Literature review on evaluation and prediction methods of inland vessel manoeuvrability. *Ocean Eng*. 106:458–471. doi:10.1016/j.oceaneng.2015.07.021.
- Millward A. 1989. The effect of water depth on hull form factor. *Int Shipbuilding Prog*. 36(407):283–302.
- Mucha P, el Moctar O, Dettmann T, Tenzer M. 2018. An experimental study on the effect of confined water on resistance and propulsion of an inland waterway ship. *Ocean Eng*. 167:11–22. doi:10.1016/j.oceaneng.2018.08.009.
- Nomoto K, Taguchi T, Honda K, Hirano S. 1957. On the steering qualities of ships. *Int Shipbuilding Prog*. 4:354–370. doi:10.3233/ISP-1957-43504.
- Ogawa A, Kasai H. 1978. On the mathematical model of manoeuvring motion of ships. *Int shipbuilding Prog*. 25:306–319. doi:10.3233/ISP-1978-2529202.
- Perčić M, Vladimir N, Fan A. 2021. Techno-economic assessment of alternative marine fuels for inland shipping in Croatia. *Renewable Sustainable Energy Rev*. 148:111363. doi:10.1016/j.rser.2021.111363.
- Pompée P-J. 2015. About modelling inland vessels resistance and propulsion and interaction vessel-waterway key parameters driving restricted/shallow water effects. *Proc Smart Rivers*. 2015:180–1–180–46.
- Rijkswaterstaat. 2011. Waterway guidelines 2011. Netherlands: Directorate-General for Public Works and Water Management, Rijkswaterstaat.
- Sys C, Voorde E, Vanelslander T, Hassel E. 2020. Pathways for a sustainable future inland water transport: a case study for the European inland navigation sector. *Case Stud Trans Policy*. 8:686–699. doi:10.1016/j.cstp.2020.07.013.
- United Nation. 2015. Transport trends and economics series, transport for sustainable development: the case of inland transport. New York and Geneva: ECE/TRANS/251.
- Vantorre M. 2003. Review of practical methods for assessing shallow and restricted water effects. *Proceedings of the International Conference on*

- Marine Simulation and Ship Maneuverability (MARSIM 2003), 2003 August 25–28, Kanazawa, Japan.
- Vantorre M, Delefortrie G, Eloot K, Laforce E. 2003. Experimental investigation of ship-bank interaction forces.
- Vantorre M, Eloot K, Delefortrie G, Lataie E, Candries M, Verwilligen J. 2017. Maneuvering in shallow and confined water. In: Carlton J, Jukes P, Choo YS, editors. The encyclopedia of Marine offshore engineering. USA: John Wiley & Sons, Ltd; p. 1–17.
- Wiegman B, Witte P, Spit T. 2015. Inland port performance: a statistical analysis of dutch inland ports. Transp Res Procedia. 8:145–154. doi:10.1016/j.trpro.2015.06.050.
- Xing S, Xinping Y, Bing W, Xin S. 2013. Analysis of the operational energy efficiency for inland river ships. 22:34–39. doi:10.1016/j.trd.2013.03.002.
- Yeo DJ, Rhee KP. 2006. Sensitivity analysis of submersibles' manoeuvrability and its application to the design of actuator inputs. Ocean Eng. 33:2270–2286. doi:10.1016/j.oceaneng.2005.11.015.
- Yoshimura Y, Sakurai H. 1988. Mathematical model for the manoeuvring ship motion in shallow water (3rd report: manoeuvrability of a twin-propeller Twinrudder ship). J Kansai Soc Naval Architects. 211:115–126.
- Zhang C, Ringsberg JW, Thies F. 2023. Development of a ship performance model for power estimation of inland waterway vessels. Ocean Eng. 287:115731. doi:10.1016/j.oceaneng.2023.115731.
- Zou L, Larsson L. 2013. Computational fluid dynamics (CFD) prediction of bank effects including verification and validation. J Mar Sci Technol. Sep;18:310–323. doi:10.1007/s00773-012-0209-7.

## Appendices

### Appendix A

Regression coefficients for the effect of forward speed:

$$\begin{aligned}
 \alpha_{10}^H &= -4.61E - 01 + 3.6E - 01 C_B^{-1} \\
 \alpha_{11}^H &= -1.73E - 01 + 1.14E - 02 C_B LT^{-1} \\
 \alpha_{12}^H &= 6.34E - 03 - 4.60E - 04 C_B LT^{-1} \\
 \alpha_{20}^H &= 1.36E + 00 - 6.58E - 02 LT^{-1} \\
 \alpha_{21}^H &= 2.57E - 01 - 8.96E - 02 BT^{-1} \\
 \alpha_{22}^H &= -1.91E - 02 + 6.34E - 03 BT^{-1} \\
 \beta_{10}^H &= -1.19E - 01 + 2.11E + 00 TL^{-1} \\
 \beta_{11}^H &= -3.54E - 02 + 1.95E - 01 BL^{-1} \\
 \beta_{12}^H &= 2.29E - 04 - 6.92E - 05 BT^{-1} \\
 \beta_{20}^H &= 1.34E - 01 - 2.35E + 00 TL^{-1} \\
 \beta_{21}^H &= -4.23E - 02 + 2.93E - 03 C_B LT^{-1} \\
 \beta_{22}^H &= 1.23E - 03 - 8.53E - 05 C_B LT^{-1}
 \end{aligned}
 \tag{A1}$$

The reference velocity  $V_T$ :

$$V_T = \sqrt{\frac{T_P}{\frac{1}{8} \rho \pi D_P^2}}
 \tag{A2}$$

Regression coefficients for the effect of propeller action:

$$\begin{aligned}
 \alpha_{10}^P &= 5.24E - 02 - 1.51E - 01 TB^{-1} \\
 \alpha_{11}^P &= 8.70E - 03 - 3.86E - 02 BL^{-1} \\
 \alpha_{12}^P &= -1.05E - 04 - 9.23E - 07 LB^{-1} \\
 \alpha_{20}^P &= 5.29E - 02 - 2.11E - 02 BT^{-1} \\
 \alpha_{21}^P &= -2.82E - 04 - 2.42E - 04 LB^{-1} \\
 \alpha_{22}^P &= 2.32E - 04 - 1.98E - 05 LB^{-1} \\
 \beta_{10}^P &= -4.95E - 03 + 1.25E - 01 C_B TL^{-1} \\
 \beta_{11}^P &= 1.29E - 03 - 5.37E - 03 TB^{-1} \\
 \beta_{12}^P &= -2.68E - 04 + 8.78E - 04 TB^{-1} \\
 \beta_{20}^P &= 3.81E - 03 - 1.29E - 02 C_B TB^{-1} \\
 \beta_{21}^P &= 3.44E - 03 - 1.10E - 03 BT^{-1} \\
 \beta_{22}^P &= 4.88E - 04 - 1.52E - 03 TB^{-1}
 \end{aligned}
 \tag{A3}$$

Regression coefficients for the coupled effect of forward speed and propeller action:

$$\begin{aligned}
 \alpha_{10}^{HP} &= -2.37E - 01 + 4.22E - 01 TB^{-1} \\
 \alpha_{11}^{HP} &= 2.89E - 02 - 2.20E - 03 LB^{-1} \\
 \alpha_{12}^{HP} &= -6.57E - 03 + 1.18E - 03 LB^{-1} \\
 \alpha_{20}^{HP} &= 4.19E - 01 - 4.79E - 02 LB^{-1} \\
 \alpha_{21}^{HP} &= -4.49E - 02 + 9.98E - 03 LB^{-1} \\
 \alpha_{22}^{HP} &= 1.06E - 02 - 4.24E - 02 TB^{-1} \\
 \beta_{10}^{HP} &= -2.89E - 01 + 5.71E + 00 TL^{-1} \\
 \beta_{11}^{HP} &= -1.22E - 01 + 3.53E - 01 TB^{-1} \\
 \beta_{12}^{HP} &= 7.87E - 03 - 2.33E - 02 TB^{-1} \\
 \beta_{20}^{HP} &= -9.33E - 02 + 1.57E - 02 LB^{-1} \\
 \beta_{21}^{HP} &= 2.60E - 01 - 7.95E - 01 TB^{-1} \\
 \beta_{22}^{HP} &= -1.99E - 02 + 5.98E - 02 TB^{-1}
 \end{aligned}
 \tag{A4}$$

### Appendix B

	H/T = 19.3	H/T = 1.5	H/T = 1.2		H/T = 19.3	H/T = 1.5	H/T = 1.2
Symbol				Symbol			
$X_{\beta\beta}^r$	-0.053	-0.1749	-0.3637	$m_x'$	0.006	0.0148	0.0195
$X_{rr}^r$	0.0272	0.0792	0.1055	$m_y'$	0.0929	0.2325	0.3722
$X_{\beta r}^r$	-0.014	-0.0888	-0.248	$t$	0.164	0.249	0.326
$Y_{\beta}^r$	0.221	0.6354	1.2375	$\alpha_H$	0.194	0.089	0.418
$Y_r^r$	-0.0091	-0.0227	-0.113	$x_H'$	-0.427	-0.249	-0.189
$Y_{\beta\beta\beta}^r$	0.4857	2.5353	4.2245	$w_{PO}$	0.340	0.493	0.576
$Y_{\beta\beta r}^r$	-0.2268	0.7413	3.6005	$\gamma_R$	0.230	0.357	0.293
$Y_{\beta rr}^r$	0.1562	0.286	0.7129	$\ell_R'$	-1.033	-0.538	-1.113
$Y_{rrr}^r$	0.0118	-0.0836	-0.2003	$\varepsilon$	0.987	1.189	1.823
$N_{\beta}^r$	0.0706	0.1988	0.4435				
$N_r^r$	-0.0593	-0.0654	-0.0861				
$N_{\beta\beta\beta}^r$	0.0848	0.5665	1.1277				
$N_{\beta\beta r}^r$	-0.1407	-0.6547	-0.2249				
$N_{\beta rr}^r$	0.0358	-0.0528	-0.0561				
$N_{rrr}^r$	0.0028	0.0097	-0.0522				